

3D Compton scattering imaging: study of the spectrum and contour reconstruction

Gaël Rigaud

Department of Mathematics, University of Würzburg, D-97074 Würzburg, Germany

E-mail: gael.rigaud@mathematik.uni-wuerzburg.de

August 2019

Abstract. 3D Compton scattering imaging is an upcoming concept focusing on exploiting the photons scattered, following on from the so-called Compton effect, by the atomic structure of an object under study. This phenomenon rules the collision of particles with electrons and describes their energy loss after scattering. Consequently, a monochromatic source leads to a polychromatic response on the camera. Assuming the camera to collect continuously the photons in terms of energy, we model the measured spectrum for first- and second-order scattering. The second-order scattered radiation reveals itself to be structurally smoother than the radiation of first-order. Therefore, the contours of the electron density are essentially encoded within the first-order scattering radiation and can be recovered from the full spectrum using a filtered backprojection kind inversion technique. Our main results, modeling and reconstruction scheme, are successfully implemented on synthetic and Monte-Carlo data.

1. Introduction

Since the advent of Computerized Tomography (CT), many imaging concepts have emerged and the need in imaging has grown. One can mention Single Photon Emission CT, Positron Emission Tomography or Cone-Beam CT for the standard system based on an ionising source. In these configurations, the energy has a very limited use but the idea of exploiting it in order to enhance the image quality, optimize the acquisition process or to compensate some limitations (such as limited angle issues) has led to various works [20, 2, 29, 11, 34, 24, 15, 14].

Computerized Tomography (CT) is a well-established and widely used technique which images an object by exploiting the properties of penetration of the x-rays. Due to the interactions of the photons with the atomic structure, the matter will resist to the propagation of the photon beam, denoted by its intensity $I(\mathbf{x}, \theta)$ at position \mathbf{x} and in direction θ , following the stationary transport equation

$$\theta \cdot \nabla_{\mathbf{x}} I(\mathbf{x}, \theta) + \mu_E(\mathbf{x}) I(\mathbf{x}, \theta) = 0, \quad \mathbf{x} \in \Omega \subset \mathbb{R}^3$$

with E the energy of the beam. The resistance of the matter is symbolized by the lineic attenuation coefficient $\mu_E(\mathbf{x})$. Solving this ordinary equation leads to the well-known Beer-Lambert law

$$I(\mathbf{y}) = I(\mathbf{x}) e^{-\int_{\mathbf{x} \rightarrow \mathbf{y}} \mu_E},$$

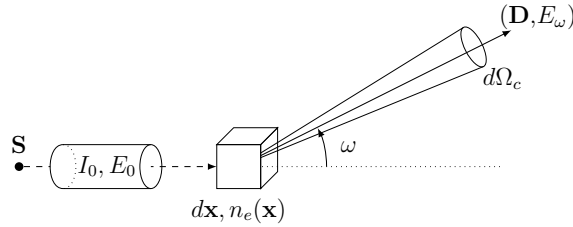


Figure 1. Geometry of Compton scattering: the incident photon energy E_0 yields a part of its energy to an electron and is scattered with an angle ω .

with $\mathbf{x} \rightarrow \mathbf{y}$ denotes the straight line $\{\mathbf{x} + t(\mathbf{y} - \mathbf{x}), t \in [0, 1]\}$. It describes the loss of intensities along the path \mathbf{x} to \mathbf{y} . In two dimensions, it is then standard to interpret the measurement of the intensity in a CT-scan using the Radon transform, which maps the attenuation map $\mu_E(x)$ into its line integrals, *i.e.*

$$\left(\ln \frac{I(\mathbf{s}, \theta)}{I(\mathbf{d}, \theta)} = \right) g(p, \theta) = \mathcal{R}\mu_E(p, \theta) = \int_{\Omega} \mu_E(x) \delta(p - x \cdot \theta) dx \quad (1)$$

with $(p, \theta) \in \mathbb{R} \times S^1$ and where \mathbf{s} and \mathbf{d} stand for the position of the source and of a camera. The task to recover μ_E from the data $g(p, \theta)$ can be achieved by various techniques such as the filtered back-projection (FBP) which regularizes the inversion formula of the Radon transform, *i.e.*

$$\mu_E(x) = \frac{1}{4\pi} \mathcal{R}^* (\mathcal{I}^{-1} g) (x)$$

with \mathcal{R}^* the L_2 -adjoint (back-projection) operator of \mathcal{R} and \mathcal{I}^{-1} the Riesz potential of order -1 .

When one focuses on the physics between the matter and the photons, four types of interactions come out: Thomson-Rayleigh scattering, photoelectric absorption, Compton scattering and pair production. In the classic range of applications of the x-rays or γ -rays, [50, 500] keV, the photoelectric absorption and the Compton scattering are the dominant phenomena which leads to a model for the lineic attenuation factor due to Stonestrom et al. [33] which writes

$$\mu_E(\mathbf{x}) = E^{-3} \lambda_{PE}(\mathbf{x}) + \sigma(E) n_e(\mathbf{x}) \quad (2)$$

where λ_{PE} is a factor depending on the materials and symbolizing the photoelectric absorption, $\sigma(E)$ the total-cross section of the Compton effect at energy E and n_e the electron density at \mathbf{x} .

The Compton effect stands for the collision of a photon with an electron. The photon transfers a part of its energy E_0 to the electron. The electron suffers then a recoil and the photon is then scattered of an (scattering) angle ω with the axis of propagation, see Fig. 1. The energy of the photon after scattering is expressed by the Compton formula [9],

$$E_\omega = \frac{E_0}{1 + \frac{E_0}{mc^2}(1 - \cos \omega)}, \quad (3)$$

where $mc^2 = 511$ keV represents the energy of an electron at rest.

The recent development of camera able to measure accurately the energy of incoming photons opens the way to an innovative 3D imaging concept, Compton

scattering imaging (abbreviated here by CSI). Although the technology of such detectors has not yet reached the same level of maturity as the one used in conventional imaging (CT, SPECT, PET), scientists have proposed and studied in the last decades different bi-dimensional systems, called Compton scattering tomography (CST), see e.g. [23, 27, 7, 1, 3, 5, 6, 8, 12, 13, 16, 19, 25, 4, 17, 30]. It is also possible to consider interior sources, for instance via the insertion of radiotracers like in SPECT. Then considering collimated detectors, it is possible to model the scattered flux through conical Radon transforms, see for instance [26, 28]. However, in this work, we consider only systems with external sources.

In this paper we assume that the source is monochromatic, *i.e.* it emits photons with same energy E_0 . For sufficiently large E_0 , larger than 80keV in medical applications, the Compton effect represents a substantial part of the radiation as more of 70% of the emitted radiation is scattered within the whole body. Therefore, the variation in terms of energy due to the Compton scattering, eq. (3), will produce a polychromatic response to the monochromatic impulse due to the source. We decompose the spectrum $\text{Spec}(\mathbf{d}, E)$ measured at a detector \mathbf{d} with energy E as follows

$$\text{Spec}(\mathbf{d}, E) = \sum_{i=0}^{\infty} g_i(\mathbf{d}, E). \quad (4)$$

In this equation, g_0 represents the primary radiation which crossed the object without being subject to the Compton effect. It corresponds to the signal measured in CT, eq. (1). The functions $g_i(D, E)$ corresponds to the photons that were measured at D with incoming energy E after i scattering events.

The purpose of this paper is to propose a strategy to extract features of the electron density n_e from the spectrum in eq. (4). The main idea arises from the smoothness properties of the operators modeling the scattered radiations at various orders. It appears that the first scattering encodes the richest information about the contours while the scattering of higher orders lead to much smoother data. To make our point but also for the sake of implementation, we focus on the first and second scattering only, which means g_1 and g_2 . g_0 is also discarded as it brings no information related to the energy although the primary radiation could be used as rich supplementary information in the future.

The manuscript is organized as follows: we first recall the results from [31] which provides the modeling of the first scattering, g_1 , and a reconstruction strategy based on contour extraction. Then we develop an analytic modeling for the second-order scattered radiation. The study of these two parts of the spectrum under Fourier integral operators shows that g_2 is substantially smoother than g_1 on the Sobolev scale. It follows that the contour based strategy proposed in [31] can be straightforwardly applied to the more general case of the full spectrum. The various modelings as well as the reconstruction technique are validated using Monte-Carlo simulations.

2. First-order scattering and toric Radon transforms

In this section, the first order scattering is characterized by a toric Radon transform. Let consider an "emission" point \mathbf{m} and a "receiver" point \mathbf{n} . The photon beam emitted by \mathbf{m} travels in the direction $\mathbf{n} - \mathbf{m}$ within a solid angle $d\Omega_c$, see Figure 1. The nature of the photon emission leads its intensity to reduce proportionally to the square of the travelled distance, the *photometric dispersion*, and exponentially due to the resistance of the matter to the propagation of light, the *attenuation factor* or

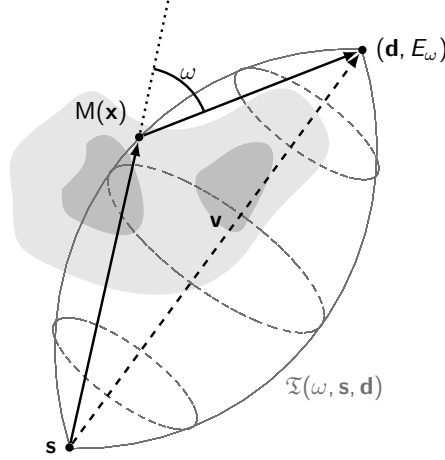


Figure 2. Geometric representation of the torus $\mathfrak{T}(\theta, E_\omega)$ in blue oriented by $\theta \in S^2$ and scaled by the scattering angle ω with $\widehat{\mathbf{SMD}} = \widehat{\mathbf{SND}} = \pi - \omega$ for all points $\mathbf{M}, \mathbf{N} \in \mathfrak{T}(\theta, E_\omega)$. The red arrows symbolize illustrations of the flight of a measured scattered photon.

Beer-Lambert law. To represent these two physical factors, we define the following mapping of the attenuation map μ_E

$$A_E(\mathbf{m}, \mathbf{n}) := \|\mathbf{n} - \mathbf{m}\|^{-2} \exp\left(-\|\mathbf{n} - \mathbf{m}\| \int_0^1 \mu_E\left(\mathbf{m} + t \frac{(\mathbf{n} - \mathbf{m})}{\|\mathbf{n} - \mathbf{m}\|}\right) dt\right).$$

Using this notation and considering a ionising source \mathbf{s} with energy E_0 and photon beam intensity I_0 , the variation of the number of photons N_c scattered at \mathbf{x} and detected at \mathbf{d} with energy E_ω , see [10], can be expressed as

$$dN_c = \frac{I_0 r_e^2}{4} P(\omega) A_{E_0}(\mathbf{s}, \mathbf{x}) A_{E_\omega}(\mathbf{x}, \mathbf{d}) n_e(\mathbf{x}) d\mathbf{x}, \quad (5)$$

where $P(\omega)$ stands for the Klein-Nishina probability [21], r_e is the classical radius of an electron. This formula describes the evolution of the first scattered radiation which is detected at a given energy and at a given detector position.

Due to the Compton formula eq. (3), the scattered energy E_ω corresponds to only one scattering angle ω and thus delivers a specific geometry when focusing on the first scattering. Indeed, all scattering points $\mathbf{M}(\mathbf{x})$ responsible for a detected scattered photon at energy E_ω belongs to

$$\mathfrak{T}(\omega, \mathbf{s}, \mathbf{d}) = \{\angle(\mathbf{x} - \mathbf{s}, \mathbf{d} - \mathbf{x}) = \pi - \omega\}$$

with $\angle(\cdot, \cdot)$ the angle between two vectors. As depicted by Figure 2, this set corresponds to a part of a spindle torus. More precisely, $\mathfrak{T}(\omega, \mathbf{s}, \mathbf{d})$ denotes the *lemon* part of the spindle torus for $\omega \in [0, \frac{\pi}{2}]$ and to its *apple* part for $\omega \in [\frac{\pi}{2}, \pi]$, see Figure 3. Assuming now \mathbf{d} to be a *point* detector and integrating over $\Omega := \text{dom}(n_e)$ the equation (5), one obtains an integral representation of the detected first scattered radiation, *i.e.*

$$g_1(\mathbf{s}, \mathbf{d}, E_\omega) = N_c(\mathbf{s}, \mathbf{d}, E_\omega) \propto \int_{\mathbf{x} \in \mathfrak{T}(\omega, \mathbf{s}, \mathbf{d})} A_{E_0}(\mathbf{s}, \mathbf{x}) A_{E_\omega}(\mathbf{x}, \mathbf{d}) n_e(\mathbf{x}) d\mathbf{x}.$$

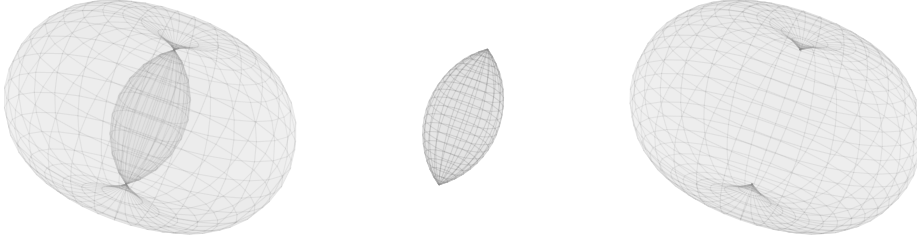


Figure 3. A complete spindle torus (left), its inside part often called *lemon* (middle) and its outside part often called *apple* (right).

As proven into [31], the quantities $N_c(\mathbf{s}, \mathbf{d}, E_\omega)$ can be interpreted as a weighted toric Radon transform,

$$N_c(\mathbf{s}, \mathbf{d}, E_\omega) = \mathcal{T}(n_e)(p, \mathbf{s}, \mathbf{d}) = \int_{\Omega} w_c(\mathbf{x}; p, \mathbf{s}, \mathbf{d}) n_e(\mathbf{x}) \delta(p - \phi(\mathbf{x}, \mathbf{s}, \mathbf{d})) d\mathbf{x}$$

with $p = \cot \omega$, $w_c = A_{E_0} \cdot A_{E_\omega}$ and the phase given by

$$\phi(\mathbf{x}, \mathbf{s}, \mathbf{d}) = \frac{(\mathbf{x} - \mathbf{s}) \cdot (\mathbf{d} - \mathbf{s}) - \|\mathbf{x} - \mathbf{s}\|^2}{\sqrt{\|\mathbf{d} - \mathbf{s}\|^2 \|\mathbf{x} - \mathbf{s}\|^2 - ((\mathbf{x} - \mathbf{s}) \cdot (\mathbf{d} - \mathbf{s}))^2}}.$$

To simplify the study but also for the sake of potential applications, we propose to fix the source \mathbf{s} . The induced modalities will then have the advantage to avoid any rotation/displacement of the source and thus enable fast acquisition time. In this case, for $\mathbf{v} = \mathbf{d} - \mathbf{s}$ and $\mathbf{y} = \mathbf{x} - \mathbf{s}$, the phase simplifies to

$$\phi(\mathbf{y}, \mathbf{v}) = \frac{\mathbf{y} \cdot \mathbf{v} - \|\mathbf{y}\|^2}{\sqrt{\|\mathbf{v}\|^2 \|\mathbf{y}\|^2 - (\mathbf{y} \cdot \mathbf{v})^2}}$$

and the first scattering radiation can be modelled by

$$g_1(\mathbf{d}, E_\omega) = \mathcal{T}(n_e)(p, \mathbf{v}) = \int_{\Omega} w_c(\mathbf{y}; p, \mathbf{v}) n_e(\mathbf{y}) \delta(p - \phi(\mathbf{y}, \mathbf{v})) d\mathbf{y}.$$

We define \mathbb{V} as the domain of definition of \mathbf{v} . We voluntarily kept the same notation between both cases \mathbf{s} fixed or not for the sake of simplicity. One can also consider the adjoint operator in a weighted L_2 space, also called here a weighted back-projection operator

$$\mathcal{T}_b^* g(\mathbf{x}) = \int_{\Theta} b(\mathbf{x}, \theta) g(\phi(\mathbf{x}, \mathbf{v}), \mathbf{v}) d\sigma(\mathbf{v})$$

with $b(\mathbf{x}, \theta)$ a positive weight function, Θ the space of the displacement of the detector w.r.t the source and $d\sigma(\mathbf{v})$ the associated measure.

The inverse problem to solve $g = \mathcal{T}(n_e)$ is very difficult problem since first of all, \mathcal{T} is a non-linear operator w.r.t the electron density n_e . Indeed the weight w_c is an operator of the lineic attenuation factor which is also a function of n_e , see eq. (2). Non-linear iterative techniques such as the Landweber iteration or the Kaczmarz's method could provide satisfactory reconstruction of n_e but at the cost of a tremendous

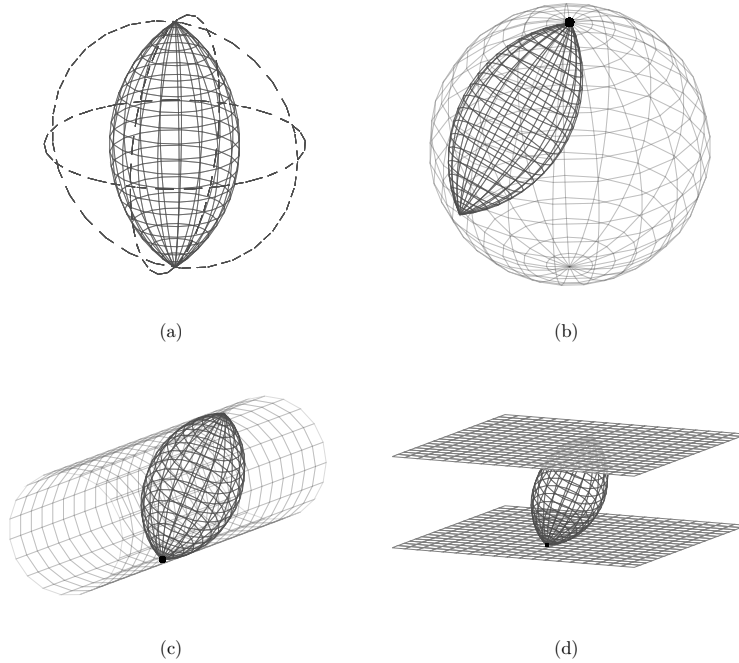


Figure 4. Four potential configurations of modalities on 3D CSI: (a) the source and one detector rotates around the object along a sphere see [37]; (b)-(c)-(d) the source is fixed and a set of detectors are located on a sphere (a), on a cylinder (b) or on two planes (c). The position of the source is not important as long as it remains outside the object.

computation time. Deep learning techniques could be used but the lack of large dataset with real/ground truth measurement prevents any training step. A first strategy was proposed in [31] for extracting the contours of n_e from $g = \mathcal{T}(n_e)$ using the following filtered backprojection formula:

$$\mathcal{K}n_e := \frac{-1}{8\pi^2} \mathcal{T}_b^* \partial_p^2 g = n_e + \mathcal{E}n_e \quad (6)$$

with \mathcal{E} a C^∞ -smooth operator and $b(\mathbf{x}, \mathbf{v}) = h(\mathbf{x}, \mathbf{v})(w_c(\mathbf{x}, \mathbf{x}, \mathbf{v}))^{-1}$ in which

$$h(\mathbf{x}, \mathbf{v}) = \left| \det \begin{pmatrix} \nabla_{\mathbf{x}} \phi(\mathbf{x}, \mathbf{v}) \\ \partial_{v_1} \nabla_{\mathbf{x}} \phi(\mathbf{x}, \mathbf{v}) \\ \partial_{v_2} \nabla_{\mathbf{x}} \phi(\mathbf{x}, \mathbf{v}) \end{pmatrix} \right|$$

is assumed $\neq 0$. The contours (or high variations) of n_e are finally recovered by applying any differential operator (gradient, laplacian, wavelets, etc). The advantage of this approach is to not require specific geometry for the displacement/position of the detectors since no structure or invariances are assumed. We can then apply the approach for various architectures of 3D CSI, see Figure 4.

Eq. (6) assumes the weight w_c to be C^∞ -smooth in order to ensure the smoothness of \mathcal{E} . This is an issue for our problem since assuming n_e to be a L_2 function with contours (singularities) will lead to a non-smooth weight w_c . However, as pointed out in [31], this can be circumvented in practice by decorrelating w_c and n_e . One

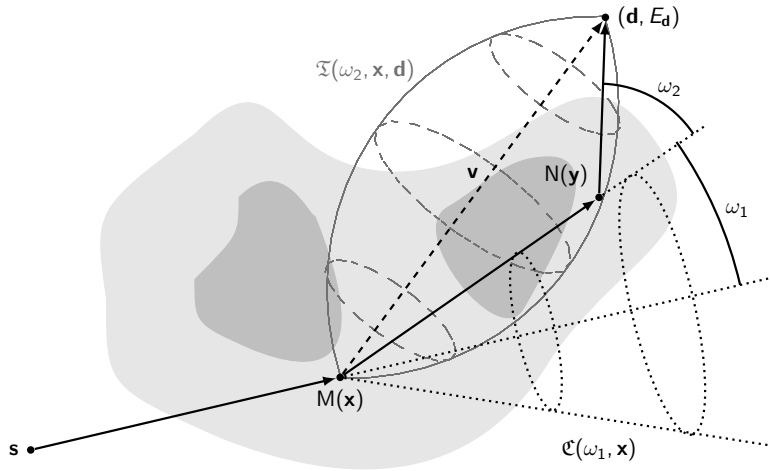


Figure 5. Geometry of the second-order scattering: a first scattering point M becomes a new source regarding the next scattering event and emits photons with energy E_{ω_1} along corresponding cones $\mathcal{C}(\omega_1, \mathbf{x})$. Beside the next scattering event occurs with an angle ω_2 leading to a scattering site N belonging to the corresponding spindle torus $\mathcal{T}(\omega_2, \mathbf{x}, \mathbf{d})$. Thence, N belongs to the intersection between the cone and the spindle torus.

can first assume w_c to be smooth and n_e to be a C^∞ -smooth approximation of a sharp-edges function $f \in L_2$. This approach is detailed and argued in Section 4, while Section 5 provides simulations of the first scattering data g_1 compared with Monte-Carlo simulations as well as reconstructions of the electron density n_e and its contours.

3. Modeling the second order scattered radiation

In this section we derive an integral representation of the part of second-order scattering in the measured spectrum. The higher orders are difficult to handle but we expect a similar approach for the higher-orders (larger than 2), this is why we will postulate the extension of the results for higher orders.

The derivation of the second scattering will use the modelling of the first scattering seen above. In this case, a measured photon is scattered twice instead of once before to be detected. We denote by $M(\mathbf{x})$ and $N(\mathbf{y})$ the first and second scattering points respectively and by ω_1 and ω_2 the first and second scattering angles respectively. The keyidea is to consider each first scattering point as a new polychromatic *source* with respect to the second scattering points and detectors.

Let us consider a detector \mathbf{d} with a detected energy E_d . Due to the Compton formula, the scattering angles must satisfy

$$\cos \omega_1 + \cos \omega_2 = 2 - mc^2 \left(\frac{1}{E_d} - \frac{1}{E_0} \right) =: \lambda(E_d) \in (0, 2). \quad (7)$$

The boundaries 0 and 2 are here excluded since they correspond to the degenerated

cases - primary ($\omega = 0$) and backscattered ($\omega = \pi$) radiation - of the torus. In consequence, the second scattering angle will be expressed as a function of the first one:

$$\omega_2(\omega_1) = \arccos(\lambda(E_{\mathbf{d}}) - \cos \omega_1).$$

The first angle w_1 means that a photon arriving at $M(\mathbf{x})$ with energy E_0 is scattered by an angle ω_1 and has afterwards an energy E_{ω_1} . Such photons belong then to the cone with aperture ω_1 , vertex $M(\mathbf{x})$ and direction $\mathbf{x} - \mathbf{s}$, i.e. to the cone

$$\mathfrak{C}(\omega_1, \mathbf{x}) := \{\mathbf{y} \in \mathbb{R}^3 : \psi(\mathbf{y}, \mathbf{x}) = \cos \omega_1\}$$

with phase

$$\psi(\mathbf{y}, \mathbf{x}) = \frac{\mathbf{y} - \mathbf{x}}{\|\mathbf{y} - \mathbf{x}\|} \cdot \frac{\mathbf{x} - \mathbf{s}}{\|\mathbf{x} - \mathbf{s}\|}.$$

This phase leads to a standard representation of the cone, *i.e.*

$$\mathfrak{C}(\omega_1, \mathbf{x}) = \left\{ \mathbf{x} + \frac{t}{\cos \omega_1} R_1 \begin{pmatrix} \sin \omega_1 \cos \varphi \\ \sin \omega_1 \sin \varphi \\ \cos \omega_1 \end{pmatrix} : t \in \mathbb{R}^+, \varphi \in [0, 2\pi[\right\}$$

with R_1 the rotation matrix which maps $\frac{\mathbf{d} - \mathbf{x}}{\|\mathbf{d} - \mathbf{x}\|}$ into $\frac{\mathbf{x} - \mathbf{s}}{\|\mathbf{x} - \mathbf{s}\|}$. Such a matrix can be computed using the Rodrigues formula.

The second angle w_2 means that a photon arriving at $N(\mathbf{y})$ with energy E_{ω_1} is scattered by an angle ω_2 and is afterwards detected at \mathbf{d} with an energy $E_{\mathbf{d}}$. As seen in the previous section, such photons belong to the torus with fixed points \mathbf{x} and \mathbf{d} , $\mathfrak{T}(\omega_2, \mathbf{x}, \mathbf{d})$, such that

$$\cot \omega_2(\omega_1) = \phi(\mathbf{y}, \mathbf{x}, \mathbf{d}).$$

A parametric representation of the spindle torus is given in [31] and writes

$$\mathfrak{T}(\omega_2, \mathbf{x}, \mathbf{d}) = \left\{ \mathbf{x} + \|\mathbf{d} - \mathbf{x}\| \frac{\sin(\omega_2 - \alpha)}{\sin \omega_2} R_2 \begin{pmatrix} \sin \alpha \cos \beta \\ \sin \alpha \sin \beta \\ \cos \alpha \end{pmatrix} : \alpha \in [0, \omega_2], \beta \in [0, 2\pi[\right\}$$

with R_2 the rotation matrix which maps $e_z = (0, 0, 1)^T$ into $\frac{\mathbf{d} - \mathbf{x}}{\|\mathbf{d} - \mathbf{x}\|}$. Shifting the torus around \mathbf{x} , it can be expressed as a unit vector multiplied by the radius

$$r(\omega_2, \alpha) = \|\mathbf{d} - \mathbf{x}\| \left(\cos \alpha - \frac{\sqrt{1 - \cos^2 \alpha}}{\tan \omega_2} \right).$$

Since the new *source* $M(\mathbf{x})$ emits photons with various energy in the corresponding cone, the Compton formula and the relationship $\omega_2(\omega_1)$ implies that a photon detected at \mathbf{d} with energy $E_{\mathbf{d}}$ and scattered at $M(\mathbf{x})$ with angle ω_1 must belong to the intersection

$$\mathbf{y} \in \mathfrak{T}(\omega_2(\omega_1), \mathbf{x}, \mathbf{d}) \cap \mathfrak{C}(\omega_1, \mathbf{x}).$$

This intersection and the principle described above is depicted in Figure 5.

To simplify the analysis, we consider the torus to be oriented in the direction e_z , which is achieved by applying the reverse matrix R_2^{-1} . In this setting, $\cos \alpha$ corresponds to the third component of the normalized vector. Since we are interested in the intersection of the cone and of the torus, one gets

$$\cos \alpha = R_1(3, 1) \sin \omega_1 \cos \varphi + R_1(3, 2) \sin \omega_1 \sin \varphi + R_1(3, 3) \cos \omega_1 =: z_{\cap}$$

with $R_1(3, \cdot)$ the third row of the rotation matrix R_1 . Using the parametrisation of the cone, one gets for the intersection, the following radius

$$r_\cap := \|\mathbf{d} - \mathbf{x}\| \left(z_\cap - \frac{\sqrt{1 - z_\cap^2}}{\tan \omega_2} \right) \quad (8)$$

and thus

$$\mathbf{y}_\cap = \mathbf{x} + r_\cap R_2 R_1 \begin{pmatrix} \sin \omega_1 \cos \varphi \\ \sin \omega_1 \sin \varphi \\ \cos \omega_1 \end{pmatrix} \quad \text{if } r_\cap > 0. \quad (9)$$

Since the torus is oriented (\mathbf{x} to \mathbf{d}), we discard the intersection between the cone and the opposite torus which corresponds to negative radii in order to fit the physics. Practically we can ignore them since they lead to detected energies outside the considered range. Also, the case $r_\cap = 0$ is discarded as it is physically impossible and would correspond to two successive scattering occurring at the exact same location. We have now the tools to give the first result of this paper.

Theorem 3.1. *Considering an electron density function $n_e(\mathbf{x})$ with compact support Ω , a monochromatic source \mathbf{s} with energy E_0 as well as a detector \mathbf{d} both located outside Ω . Then, the number of detected photons scattered twice arriving with an energy $E_{\mathbf{d}}$ are given by*

$$g_2(\mathbf{d}, E_{\mathbf{d}}) = \int_{\Omega} \int_0^{2\pi} \int_0^\pi w_2(\mathbf{s}, \mathbf{x}, \mathbf{y}_\cap, \mathbf{d}, \omega_1, \varphi) n_e(\mathbf{x}) n_e(\mathbf{y}_\cap) dS_\cap(\omega_1, \varphi) d\mathbf{x} \quad (10)$$

with the physical factors symbolized by

$$w_2(\mathbf{s}, \mathbf{x}, \mathbf{y}_\cap, \mathbf{d}, \omega_1, \varphi) = A_{E_0}(\mathbf{s}, \mathbf{x}) A_{E_{\omega_1}}(\mathbf{x}, \mathbf{y}_\cap) A_{E_{\omega_2}}(\mathbf{y}_\cap, \mathbf{d})$$

and the differential form of the intersection given by

$$dS_\cap(\omega_1, \varphi) = r_\cap \sqrt{\sin^2 \omega_1 (r_\cap^2 + (\partial_{\omega_1} r_\cap)^2) + (\partial_\varphi r_\cap)^2} d\omega_1 d\varphi$$

in which \mathbf{y}_\cap and r_\cap are described in eqs (9) and (8).

Proof. The structure follows on from the physics of Compton scattering. Akin to the first scattering, the variation of photon scattered twice can be expressed as

$$d^2 g_2 = I_0 \left(\frac{1}{2} r_e \right)^4 P(\omega_1) P(\omega_2) A_{E_0}(\mathbf{s}, \mathbf{x}) A_{E_{\omega_1}}(\mathbf{x}, \mathbf{y}) A_{E_{\omega_2}}(\mathbf{y}, \mathbf{d}) n_e(\mathbf{x}) n_e(\mathbf{y}) d\mathbf{x} d\mathbf{y}.$$

Therefore, ignoring some physical constants and based on our development above, one can integrate to get the theoretical number of photons detected at \mathbf{d} with energy $E_{\mathbf{d}}$ after two scattering events,

$$g_2(\mathbf{d}, E_{\mathbf{d}}) = \int_{\Omega} \int_{\mathfrak{T}(\omega_2(\omega_1), \mathbf{x}, \mathbf{d}) \cap \mathfrak{C}(\omega_1, \mathbf{x})} A_{E_0}(\mathbf{s}, \mathbf{x}) A_{E_{\omega_1}}(\mathbf{x}, \mathbf{y}) A_{E_{\omega_2}}(\mathbf{y}, \mathbf{d}) n_e(\mathbf{x}) n_e(\mathbf{y}) d\mathbf{y} d\mathbf{x}.$$

This intersection is characterized by eqs. (9) and (8). We still have to compute the differential form along the intersection and thus

$$\|\partial_{\omega_1} \mathbf{y}_\cap \wedge \partial_\varphi \mathbf{y}_\cap\|$$

for $\mathbf{x}, \mathbf{d}, \mathbf{s}$ given. First, one can compute

$$\partial_\varphi \mathbf{y}_\cap = R_2 R_1 \left(r_\cap \begin{pmatrix} -\sin \omega_1 \sin \varphi \\ \sin \omega_1 \cos \varphi \\ 0 \end{pmatrix} + \partial_\varphi r_\cap \begin{pmatrix} \sin \omega_1 \cos \varphi \\ \sin \omega_1 \sin \varphi \\ \cos \omega_1 \end{pmatrix} \right)$$

and

$$\partial_{\omega_1} \mathbf{y}_\cap = R_2 R_1 \left(r_\cap \begin{pmatrix} \cos \omega_1 \cos \varphi \\ \cos \omega_1 \sin \varphi \\ -\sin \omega_1 \end{pmatrix} + \partial_{\omega_1} r_\cap \begin{pmatrix} \sin \omega_1 \cos \varphi \\ \sin \omega_1 \sin \varphi \\ \cos \omega_1 \end{pmatrix} \right).$$

This leads to

$$\begin{aligned} \partial_\varphi \mathbf{y}_\cap \wedge \partial_{\omega_1} \mathbf{y}_\cap &= R_2 R_1 \left(r_\cap^2 \begin{pmatrix} \sin^2 \omega_1 \cos \varphi \\ \sin^2 \omega_1 \sin \varphi \\ \cos \omega_1 \sin \omega_1 \end{pmatrix} + r_\cap \partial_\varphi r_\cap \begin{pmatrix} \sin \varphi \\ -\cos \varphi \\ 0 \end{pmatrix} \right. \\ &\quad \left. + r_\cap \partial_{\omega_1} r_\cap \begin{pmatrix} -\cos \omega_1 \sin \omega_1 \cos \varphi \\ -\cos \omega_1 \sin \omega_1 \sin \varphi \\ \sin^2 \omega_1 \end{pmatrix} \right). \end{aligned}$$

Since the rotation matrices do not change the norm, they can be ignored in the computation of the norm. After some computations, one gets

$$\|\partial_{\omega_1} \mathbf{y}_\cap \wedge \partial_\varphi \mathbf{y}_\cap\| = r_\cap \sqrt{\sin^2 \omega_1 (r_\cap^2 + (\partial_{\omega_1} r_\cap)^2) + (\partial_\varphi r_\cap)^2}$$

where

$$\begin{aligned} \partial_{\omega_1} r_\cap &= (z_\cap)_{\omega_1} \left(1 + \cot \omega_2 \frac{z_\cap}{\sqrt{1 - z_\cap^2}} \right) - \frac{\sin \omega_1}{\sin^3 \omega_2} \sqrt{1 - z_\cap^2} \\ \partial_\varphi r_\cap &= (z_\cap)_\varphi \left(1 + \cot \omega_2 \frac{z_\cap}{\sqrt{1 - z_\cap^2}} \right) \end{aligned}$$

in which

$$\begin{aligned} (z_\cap)_{\omega_1} &= R_1(3, 1) \cos \omega_1 \cos \varphi + R_1(3, 2) \cos \omega_1 \sin \varphi - R_1(3, 3) \sin \omega_1 \\ (z_\cap)_\varphi &= R_1(3, 2) \sin \omega_1 \cos \varphi - R_1(3, 1) \sin \omega_1 \sin \varphi. \end{aligned}$$

This ends the proof. \square

This Theorem delivers an integral representation for the second scattering in any configuration/architecture for the displacement/location of the source and detectors. The modeling will be validated and compared to Monte-Carlo simulations in section 5.

The next section discusses the smoothness properties of the different orders of Compton scattering within the spectrum.

4. Smoothness properties within the spectrum and contour reconstruction

This section sets our operators in the context of Fourier integral operators. For modalities involving Compton scattering, some cases were already studied in 2D [36] and 3D [38] using microlocal analysis. As mentioned above, the whole theory assumes the weight function to be smooth. In our case, this implies that the electron density

n_e must be considered in C^∞ . We, however, use a first result on the continuity of our operator \mathcal{T} in L_2 .

Theorem 4.1. *For \mathbf{s} and \mathbf{d} fixed, the spindle tori $\mathfrak{T}(\omega, \mathbf{s}, \mathbf{d})$ are one-to-one with $\mathbb{R}^3 \setminus \{\mathbf{s} + t(\mathbf{d} - \mathbf{s}), t \in \mathbb{R}\}$.*

Proof. First, we discard the degenerate case of the spindle torus which occurs when $\omega = 0$ (there is no scattering event, only primary radiation) and corresponds to the line $\{\mathbf{s} + t(\mathbf{d} - \mathbf{s}), t \in \mathbb{R}\}$.

The parameter representation of the spindle torus is given by

$$\mathfrak{T}(\omega, \mathbf{s}, \mathbf{d}) = \left\{ \mathbf{x} = \mathbf{s} + \|\mathbf{d} - \mathbf{s}\| \frac{\sin(\omega - \alpha)}{\sin \omega} R_2 \begin{pmatrix} \sin \alpha \cos \beta \\ \sin \alpha \sin \beta \\ \cos \alpha \end{pmatrix} : \alpha \in [0, \omega], \beta \in [0, 2\pi[\right\}$$

with $p = \cot \omega$ and R_2 the rotation matrix which maps $e_z = (0, 0, 1)^T$ into $\frac{\mathbf{d} - \mathbf{s}}{\|\mathbf{d} - \mathbf{s}\|}$. For \mathbf{s} and \mathbf{d} fixed, it is clear that

$$R_2 \begin{pmatrix} \sin \alpha \cos \beta \\ \sin \alpha \sin \beta \\ \cos \alpha \end{pmatrix}$$

is one-to-one with the unit sphere. This is why each $\mathbf{x} \in \mathbb{R}^3$ corresponds to only one pair (α, β) . Now, since $\frac{\sin(\omega - \alpha)}{\sin \omega}$ is defined for $\omega > \alpha$, the norm of the vector $\mathbf{x} - \mathbf{s}$ is a bijective function on ω .

Therefore, the spindle torus parametrized by (ω, α, β) is one-to-one with $\mathbb{R}^3 \setminus \{\mathbf{s} + t(\mathbf{d} - \mathbf{s}), t \in \mathbb{R}\}$. \square

Theorem 4.2. *Denoting by $\mathcal{T}_{\mathbf{d}}$, the restriction of \mathcal{T} to one detector \mathbf{d} and a given source \mathbf{s} , then*

$$\mathcal{T}_{\mathbf{d}} : L_2(\Omega) \rightarrow L_2(\mathbb{R}).$$

is continuous.

Proof. From [31], we know that

$$\mathcal{T}n_e(p, \mathbf{v}) = \int_0^{2\pi} \int_0^\omega w_c(\mathbf{y}(p, \alpha, \beta); p, \mathbf{v}) n_e(\mathbf{y}(p, \alpha, \beta)) J(p, \alpha, \beta) d\alpha d\beta$$

with $p = \cot \omega$, $\mathbf{v} = \mathbf{d} - \mathbf{s}$ and J the appropriate Jacobian given in [31]. Using the Cauchy-Schwarz inequality, one gets

$$\begin{aligned} |\mathcal{T}n_e(p, \mathbf{v})|^2 &\leq \int_0^{2\pi} \int_0^\omega (w_c(\mathbf{y}(p, \alpha, \beta); p, \mathbf{v}))^2 \chi_\Omega(\alpha, \beta) J(p, \alpha, \beta) d\alpha d\beta \\ &\cdot \int_0^{2\pi} \int_0^\omega (n_e(\mathbf{y}(p, \alpha, \beta)))^2 J(p, \alpha, \beta) d\alpha d\beta \end{aligned}$$

in which χ_Ω stands for a smooth cut-off. Taking now the L_2 norm yields

$$\|\mathcal{T}n_e\|_{L_2} \leq c \int_{\mathbb{R}} \int_0^{2\pi} \int_0^\omega (n_e(\mathbf{y}(p, \alpha, \beta)))^2 J(p, \alpha, \beta) d\alpha d\beta dp$$

with

$$c = \int_{\mathbb{R}} \int_0^{2\pi} \int_0^\omega (w_c(\mathbf{y}(p, \alpha, \beta); p, \mathbf{v}))^2 \chi_\Omega(\alpha, \beta) J(p, \alpha, \beta) d\alpha d\beta dp$$

which is well-defined as the integrand is a compactly supported smooth function. Due to Theorem 4.1 and since the discarded line passing through \mathbf{s} and \mathbf{d} is negligible regarding the Lebesgue measure, one can finally apply the mapping $(p, \alpha, \beta) \mapsto \mathbf{x}$ and gets

$$\|\mathcal{T}n_e\|_{L_2}^2 \leq c \int_{\Omega} (n_e(\mathbf{x}))^2 d\mathbf{x} = c \|n_e\|_{L_2}^2.$$

□

For our approach, the operator \mathcal{T} has two main drawbacks: (i) it is non-linear in n_e as the physical factors, w_c , depends on n_e ; (ii) the properties of Fourier integral operators cannot apply if the weight function and thus n_e are not C^∞ smooth. To circumvent these difficulties, we propose for this study to decorrelate the dependence of the weight w_c w.r.t. n_e with the integrand itself. At this purpose, we assume that n_e is C^∞ smooth and that there exists a function $f \in L_2(\Omega)$ such that

$$\|f - n_e\|_{L_2(\Omega)} \leq \epsilon \ll 1.$$

Thanks to the continuity of the operator shown in Theorem 4.2, the spectral data g_1 can thus be seen as an approximation of

$$\mathcal{T}(f, n_e)(p, \mathbf{v}) = \int_{\Omega} \mathcal{W}n_e(\mathbf{x}, p, \mathbf{v}) f(\mathbf{x}) \delta(p - \phi(\mathbf{x}, \mathbf{v})) d\mathbf{x}$$

with \mathcal{W} the operator acting on the electron density and standing for the physical factors. For our study, the edges (high-variations) of the electron density n_e will be carried by the function f and we will consider the operator $\mathcal{T}(\cdot, n_e)$ instead of \mathcal{T} . Now we have the operator in a correct shape and we can recall some results from the theory on Fourier integral operators, see [35, 22].

Definition 4.3 ([22]). *Let $Y \subset \mathbb{R}^m$ and $X \subset \mathbb{R}^n$ be open subsets. A real valued function $\phi \in C^\infty(Y \times X \times \mathbb{R}^N \setminus \{0\})$ is called a phase function if*

- ϕ is positive homogeneous of degree 1 in ξ , i.e. $\phi(y, x, r\xi) = r\phi(y, x, \xi)$ for all $r > 0$.
- $(\partial_y \phi, \partial_\xi \phi)$ and $(\partial_x \phi, \partial_\xi \phi)$ do not vanish for all $(y, x, \xi) \in Y \times X \times \mathbb{R}^N \setminus \{0\}$.

A Fourier integral operator \mathcal{P} is then defined as

$$\mathcal{P}u(y) = \int e^{i\phi(y, x, \xi)} a(y, x, \xi) u(x) dx d\xi$$

where the symbol/amplitude $a(\cdot) \in C^\infty(Y \times X \times \mathbb{R}^N)$ and it satisfies:

For every compact set $K \subset Y \times X$ and for every multi-index α, β, γ , there is a constant C such that

$$|\partial_\xi^\alpha \partial_x^\beta \partial_y^\gamma a(y, x, \xi)| \leq C(1 + \|\xi\|)^{m - |\alpha|} \quad \forall x, y \in K \text{ and } \forall \xi \in \mathbb{R}^N.$$

We write then that $a \in S^m(Y \times X \times \mathbb{R}^N)$.

Theorem 4.4 ([35]). *Given a FIO \mathcal{P} with symbol*

$$a(\cdot) \in S^{m + \frac{n+m}{4} - \frac{N}{2}}(Y \times X \times \mathbb{R}^N)$$

then \mathcal{P} is a FIO of order m and maps continuously the Sobolev spaces $H^s(X)$ into $H_{loc}^{s-m}(Y)$ for every $s \in \mathbb{R}$.

Corollary 4.5. *Let $n_e \in C^\infty(\Omega)$ given with Ω an open subset of \mathbb{R}^3 . Then the operator $\mathcal{T}(\cdot, n_e) : H^s(\Omega) \mapsto H_{loc}^{s+1}(\mathbb{R} \times \mathbb{V})$ is a continuous Fourier integral operator of order -1 .*

Proof. The proof here is inspired from [18]. Using the Fourier representation of the Dirac distribution, one gets

$$\mathcal{T}(f, n_e)(p, \mathbf{v}) = \frac{1}{\sqrt{2\pi}} \int_{\Omega} \int_{\mathbb{R}} \mathcal{W}n_e(\mathbf{x}, p, \mathbf{v}) f(\mathbf{x}) e^{-i\sigma(p - \phi(\mathbf{x}, \mathbf{v}))} d\sigma d\mathbf{x}.$$

Defining the phase

$$\Phi(p, \mathbf{v}, \mathbf{x}, \sigma) = \sigma(p - \phi(\mathbf{x}, \mathbf{v})),$$

one needs to prove that $(\partial_{p, \mathbf{v}}\Phi, \partial_\sigma\Phi)$ and $(\partial_{\mathbf{x}}\Phi, \partial_\sigma\Phi)$ do not vanish for all $(p, \mathbf{v}, \mathbf{x}, \sigma) \in \mathbb{R} \times \mathbb{V} \times \Omega \times \mathbb{R} \setminus \{0\}$. It is clear that

$$\partial_\sigma\Phi = (p - \phi(\mathbf{x}, \mathbf{v}))d\sigma \quad \text{and} \quad \partial_{p, \mathbf{v}}\Phi = \sigma(dp - \partial_{\mathbf{v}}\phi(\mathbf{x}, \mathbf{v})d\mathbf{v}).$$

The second term is never zero, so $(\partial_{p, \mathbf{v}}\Phi, \partial_\sigma\Phi)$ does not vanish. Also, setting $\mathbf{y} = \mathbf{x} - \mathbf{s}$ and $\mathbf{v} = r_v\theta_v$, one can prove that

$$\nabla_{\mathbf{y}}\phi(\mathbf{y}, \mathbf{v}) = \frac{\kappa(\mathbf{y})}{(1 - \lambda^2(\mathbf{y}))^{3/2}} \left(\kappa(\mathbf{y}) - \frac{\|\mathbf{y}\|}{r_v} \right) \nabla_{\mathbf{y}}\kappa(\mathbf{y}) + \frac{\left(\nabla_{\mathbf{y}}\kappa(\mathbf{y}) - \frac{\mathbf{y}}{\|\mathbf{y}\|r_v} \right)}{\sqrt{1 - \lambda^2(\mathbf{y})}}$$

with

$$\kappa(\mathbf{y}) = \frac{\mathbf{y} \cdot \theta_v}{\|\mathbf{y}\|} \quad \text{and} \quad \nabla_{\mathbf{y}}\kappa(\mathbf{y}) = \|\mathbf{y}\|^{-1} \left(\theta_v - \kappa(\mathbf{y}) \frac{\mathbf{y}}{\|\mathbf{y}\|} \right).$$

The gradient of the phase is thus the sum of two vectors each one collinear with \mathbf{y} and θ_v respectively. Important cases here show up, first \mathbf{y} must be different from $\mathbf{0}$, which means $\mathbf{x} \neq \mathbf{s}$. This is naturally excluded by taking the source outside Ω . Then, comes the case $\kappa(\mathbf{y}) = 1$, which means \mathbf{y} and θ_v are collinear. It corresponds to the spindle torus degenerating into the straight line \mathbf{s} to \mathbf{d} (no scattering only primary radiation). This case is also excluded since $\omega > 0$ strictly or equivalently $p \neq \infty$. Since \mathbf{y} and θ_v cannot be collinear, the gradient $\nabla_{\mathbf{y}}\phi(\mathbf{y}, \mathbf{v})$ is never zero and therefore, \mathcal{T} is a FIO.

Due to the smoothness properties of the electron density, $\mathcal{W}n_e \in C^\infty$ and is thus a symbol of order 0. Given Theorem 4.4 and that $(\partial_{p, \mathbf{v}}\Phi, \partial_\sigma\phi)$ and $(\partial_{\mathbf{x}}\phi, \partial_\sigma\phi)$ do not vanish, $\mathcal{T}(\cdot, n_e)$ is thus a FIO of order

$$m = \frac{1}{2} - \frac{3+3}{4} = -1$$

and therefore maps continuously $H^s(\Omega)$ into $H_{loc}^{s+1}(\mathbb{R} \times \mathbb{V})$ where \mathbb{V} denotes the domain of definition of $\mathbf{d} - \mathbf{s}$. \square

Corollary 4.6. *Let $n_e \in C^\infty(\Omega)$ given with Ω an open subset of \mathbb{R}^3 . Then, the scattered radiation of order 2 can be understood as a continuous mapping between $H^s(\Omega)$ and $H_{loc}^{s+7/4}(\mathbb{R}^+ \times \mathbb{V})$ if the phase function*

$$\Psi(\mathbf{y}, \mathbf{x}, \mathbf{d}) := \psi(\mathbf{y}, \mathbf{x}) + \cos(\cot^{-1} \phi(\mathbf{y}, \mathbf{x}, \mathbf{d}))$$

satisfies $(\nabla_{\mathbf{x}}\Psi, \nabla_{\mathbf{y}}\Psi) \neq \mathbf{0}$.

Proof. In order to write the second scattering data g_2 as a FIO, one needs to find the corresponding phase function of the intersection between the cone and the spindle torus. The phase is delivered by our condition on the scattering angles and the energy derived from the Compton formula eq. (7). It yields

$$\psi(\mathbf{y}, \mathbf{x}) + \cos(\cot^{-1} \phi(\mathbf{y}, \mathbf{x}, \mathbf{v})) = \lambda(E_d) = \Psi(\mathbf{y}, \mathbf{x}, \mathbf{v}) \in \mathbb{R}^+.$$

Ψ inherits essentially the properties of phase of ψ and of ϕ as λ is monotone w.r.t the energy. Although it can be empirically checked, it is unclear when $(\nabla_{\mathbf{x}}\Psi, \nabla_{\mathbf{y}}\Psi) \neq \mathbf{0}$ analytically, this is why this is assumed here. With this symbolism, g_2 can be understood as an approximation of the operator

$$\mathcal{S}(f, n_e)(\lambda, \mathbf{v}) = \int_{\Omega} \int_{\Omega \setminus \{\mathbf{x}\}} w_2(\mathbf{s}, \mathbf{x}, \mathbf{y}, \mathbf{v}) f(\mathbf{x}) f(\mathbf{y}) \delta(\lambda - \Psi(\mathbf{y}, \mathbf{x}, \mathbf{v})) d\mathbf{y} d\mathbf{x}.$$

The case $\mathbf{x} = \mathbf{y}$ is discarded as it corresponds for the tori to a singularity that shows up in the definition of the phase ϕ (it was the case $\mathbf{s} = \mathbf{x}$ for the first scattering). Physically, this case cannot occur as it would imply that the same local point is responsible for two successive scattering events which is impossible. To interpret this as a FIO, we embed the variable (\mathbf{y}, \mathbf{x}) into $\mathbf{z} \in \Omega_2 := \{(\mathbf{y}, \mathbf{x}) \in \Omega \setminus \{\mathfrak{N}(\mathbf{x})\} \times \Omega\}$, with $\mathfrak{N}(\mathbf{x})$ denoting a small neighborhood around \mathbf{x} . Taking $f(\mathbf{z}) = f(\mathbf{x})f(\mathbf{y})$, it yields

$$\begin{aligned} \mathcal{S}_2(\bar{f}, n_e)(\lambda, \mathbf{v}) &= \int_{\Omega_2} \bar{w}_2(\mathbf{s}, \mathbf{z}, \mathbf{v}) \bar{f}(\mathbf{z}) \delta(\lambda - \bar{\Psi}(\mathbf{z}, \mathbf{v})) d\mathbf{z} \\ &= \int_{\Omega_2} \int_{\mathbb{R}} \bar{w}_2(\mathbf{s}, \mathbf{z}, \mathbf{v}) \bar{f}(\mathbf{z}) e^{-i\sigma(\lambda - \bar{\Psi}(\mathbf{z}, \mathbf{v}))} d\sigma d\mathbf{z} \end{aligned}$$

with \bar{w}_2 and $\bar{\Psi}$ the appropriate embedded version of w_2 and Ψ . Given Theorem 4.4 and assuming the properties of phase of $\bar{\Psi}$, \mathcal{S}_2 is a FIO of order

$$m = \frac{1}{2} - \frac{6+3}{4} = -\frac{7}{4}$$

which ends the proof. \square

Remark 4.7. *The assumption that $(\nabla_{\mathbf{x}}\Psi, \nabla_{\mathbf{y}}\Psi) \neq \mathbf{0}$ is in fact almost always satisfied. Indeed, the computation of $\nabla_{\mathbf{y}}\Psi$ is a linear combination of three vectors $\mathbf{x} - \mathbf{s}$, $\mathbf{y} - \mathbf{x}$ and $\mathbf{d} - \mathbf{x}$. Since the degenerated cases for the cone, $\mathbf{x} - \mathbf{s}$ and $\mathbf{y} - \mathbf{x}$ collinear, and for the spindle torus, $\mathbf{y} - \mathbf{x}$ and $\mathbf{d} - \mathbf{x}$ collinear, are excluded, there are two possibilities: either these three vectors are linearly independant, then Ψ inherits the property of phase of ϕ ($(\nabla_{\mathbf{x}}\Psi, \nabla_{\mathbf{y}}\Psi) \neq \mathbf{0}$), or they belong to the same plane. In the latter case, the analysis is unclear. The desired property can however be checked empirically.*

By analogy, the scattering of order k ($k > 2$) will rely on the relation

$$\sum_{i=1}^k \cos \omega_i = k - mc^2 \left(\frac{1}{E_d} - \frac{1}{E_0} \right)$$

with ω_i the i^{th} scattering angle. Unfortunately, the geometry of the scattering events becomes harder to model or even to implement. However, we expect the principle we developed for the second scattering to extend to higher orders since each additional scattering will add a new *layer* of intermediary sources. This extension is expressed in the following statement.

Hypothesis 4.8. *When focusing on the Compton scattering, the measured spectrum can be decomposed into the different scattered radiation of i^{th} order,*

$$\text{Spec}(\mathbf{d}, E) = \sum_{i=1}^{\infty} g_i(\mathbf{d}, E)$$

with g_i approximating the operator $\mathcal{T}_i(\cdot, n_e)$ which maps continuously

$$H^s(\Omega) \mapsto H_{loc}^{s+(3i+1)/4}(\text{dom}(E) \times \mathbb{V}).$$

Intuitively, the more scattering events, the smoother the corresponding part within the spectrum is.

Theorem 4.9. *Assuming the attenuation factors to be known and $f \in L_2(\Omega)$ to be a sharp version of the smooth electron density n_e , the reconstruction operator $\mathcal{T}_b^* \partial_p^2$ with the backprojection operator*

$$\mathcal{T}_b^* g(\mathbf{x}) = \int_{\mathbb{V}} (\mathcal{W}n_e(\mathbf{x}, \phi(\mathbf{x}, \mathbf{v}), \mathbf{v}))^{-1} h(\mathbf{x}, \mathbf{v}) g(\phi(\mathbf{x}, \mathbf{v}), \mathbf{v}) d\mathbf{v}$$

maps the spectrum Spec onto f up to an error $\epsilon \in H_{loc}^{3/4}(\Omega)$.

Proof. The result follows on from the smoothness properties given above and from [31]. The reconstruction operator recovers f up to a C^∞ -smooth function and acts as a FIO of order 1 on the second scattering data $g_2 \in H^{7/4}$ which is compactly supported when considering the energy E as variable instead of p . \square

Since the error ϵ produced by the reconstruction technique is smoother than f , it is possible to extract accurately the contours (jumps) of f by applying suited operators (gradient, laplacian, wavelets, etc).

Remark 4.10. *Following from [31], the weight (and thus here the attenuation factors) needs to be known to recover f and not a weighted version. In practice, a rough approximation of the weight is sufficient to recover the contours of f but the analysis of the reconstruction operator with inexact weights will be performed in future research.*

5. Simulation results

In this section, we provide simulation results for the configuration (b) in Figure 4. As explained in [31], this configuration has the advantage to minimize the acquisition time (in comparison with the configuration (a)) while delivering data without limited angle issues (in comparison with (c) and (d)). However, this latter point will depend on the resolution of the detector. For this paper, we assumed that the detector has a continuous energy resolution. In practice, a fixed energy resolution will alter the accuracy of our integral representation for the back-scattered photons ($\omega > \pi/2$) leading to inconsistent data and thus limited data artifacts. This aspect constitutes the next step of our future research.

A slice of the *scanner* is depicted in Figure 6. The monochromatic source, emitting at $E_0 = 140$ keV, is fixed and located under the object while the detectors are located on a sphere (the half-circle on the slice) of diameter equal to 40 cm. Each detector is a disk of 2mm of radius. The volume to reconstruct is represented by a

cube in the middle of $10 \times 10 \times 10 \text{cm}^3$. We consider that the source has emitted 10^{12} photons; a sufficient amount in order to limitate the Poisson noise in the Monte-Carlo data.

The electron density map is scaled on the value of the water, $3.23 \cdot 10^{23}$ electrons per cm^{-3} , noted n_w .

5.1. Comparison with Monte-Carlo data

We first compare our model of the spectrum for first- and second-order scattering with ground truth data obtained by Monte-Carlo simulation. To view the response of the different operators, we consider the well-known *point spread function*. In order to validate, the modeling of the second scattering, two *points* (small spheres of radius 2mm) are considered. Figure 6 displays the different results for one arc of detectors (the complete dataset is obtained for detectors along the complete sphere). Analytic data (middle column) are compared with ground truth data (right column). The first row shows the part of the first-scattering within the spectrum, g_1 , the second row the part of the second scattering g_2 , and the third row the spectrum (neglecting higher-order scattering) $g_1 + g_2$. The analytic spectrum and the different parts match with the realistic spectrum. One can observe some variations in the intensities which arise from the discretization of the modeling. In particular, for the Monte-Carlo simulations, the detector is no more a point but a disk of size 4mm and the detection of the energy is made on a range of energy $E \pm \Delta E$ and not a single value E . Here ΔE is set 0.25 keV. Combined together, the modeling is altered since we do not integrate over spindle torus (or over the intersection with the cone for g_2) but over a strip around the spindle torus. However, the analytical modeling is revealed to appropriately model the spectrum as shown by the reconstructions in the next paragraph.

5.2. Contour Reconstruction

We now provide the reconstructions and contour extractions for a toy object following on from the reconstruction strategy developed before. The object is a composition of spheres with electron densities $\{0, 1, 1.5, 2, 3\} \times n_w$ compactly supported in a cube of dimension $10 \times 10 \times 10 \text{cm}^3$.

The spectrum and its decomposition are depicted in Figure 7. The reconstructions are displayed in Figure 8. As anticipated, the application of the filtered back-projection type algorithm does not provide a satisfactory reconstruction of the object. This is essentially due to the physical factors which alter substantially the integral kernel. They produce *smooth* artifacts, noted $\mathcal{E}f$ in the reconstruction scheme, quite strong. By analogy with the attenuated Radon transform [32], the ill-conditioning of the reconstruction problem should increase exponentially with the intensity of the electron density which is observed in practice. The values of the electron density considered here as well as the variation of the physical factors are thus substantially amplified by the reconstruction strategy.

However, the extraction of the contours, Figure 9, enables a better visualization of the features of the object. Here, we simply take the gradient of the reconstructions from Figure 8 but more sophisticated techniques could be applied. The second column displays the contours obtained from the analytical data for g_1 . In this case, the contours are well-recovered. However, we can observe some artifacts arising from the variations of the physical factors. These artifacts turn out more prominent for

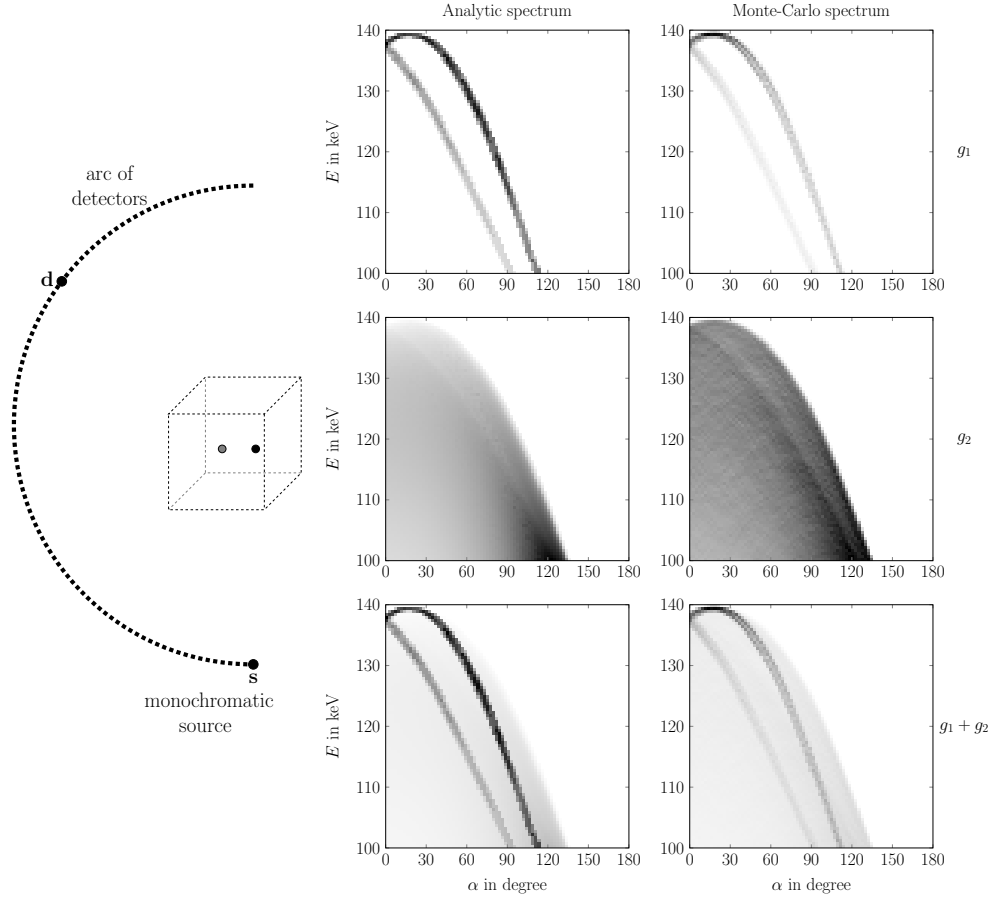


Figure 6. Illustration of the *point spread function* for the first-order scattered radiation g_1 and the second-order scattering radiation g_2 . The sketch on the left depicts the configuration: a monochromatic source is fixed and the detectors are located on a half-circle. Our volume (the cube in the center) consists of two points with intensities n_w and $2n_w$. The figures in the middle correspond to an implementation of the integral representation of the data while the ones on the right gives the corresponding Monte-Carlo data.

Monte-Carlo data in the third and fourth columns. These can be explained by the smoothing effect of the acquisition, giving that the modeling itself is in reality not the torus but a strip around the torus giving smoother behaviour of the measurement than for the analytical modeling. Thence, the contours are smoothed making the artifacts more visible. Furthermore, as developed in this paper, the contours are encoded and preserved by the first-order scattered radiation and can be recovered even when considering the second-order scattering (fourth column). The key point here is that the second scattering is smoother than the first scattering. Consequently, the second derivative ∂_p^2 in the reconstruction scheme, highlights the variations of g_1 over g_2 and leads to a reconstruction almost not hindered by the second scattering. We expect the same behaviour for higher-ordered scattered radiation in the spectrum.

Due to the computation time of the data and of the Monte-Carlo simulations,

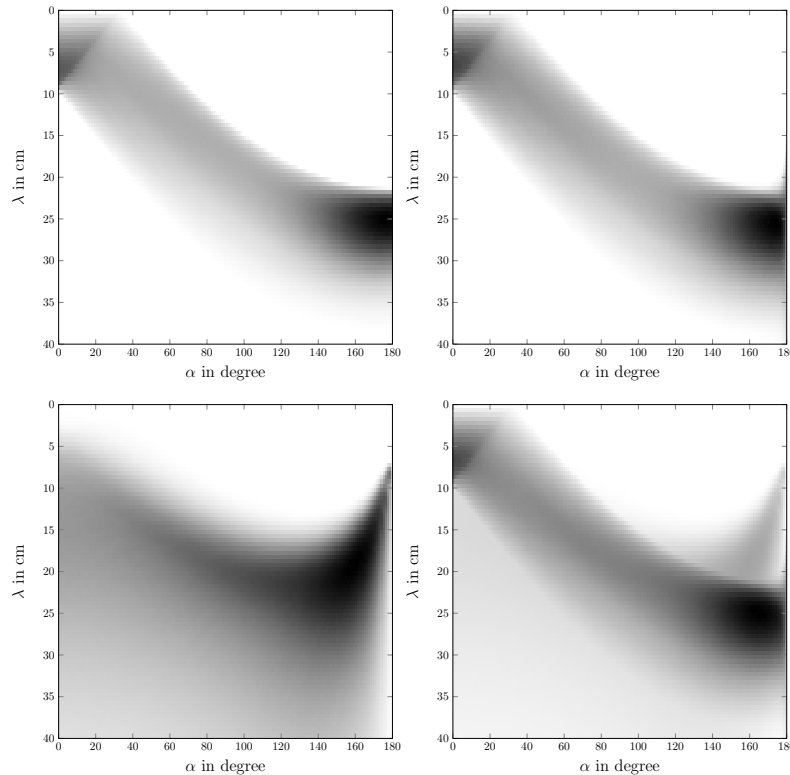


Figure 7. Different parts of the spectrum from the electron density n_e depicted in Figure 8. top left: implementation of the integral representation of g_1 ; top right: corresponding Monte-Carlo data g_1^{MC} ; bottom left: g_2^{MC} obtained by Monte-Carlo simulation; bottom right: $g_1^{MC} + g_2^{MC}$

we restricted the sampling of our toy object to $80 \times 80 \times 80$ voxels which is small for recovering contours. We expect sharper reconstructions of the edges and less prominent artifacts for higher resolution of the data.

6. Conclusion

In conclusion, we proved and tested that the contours of the object of interest are encoded essentially in the first-scattering within the spectrum. Sufficiently smooth, the rest of the spectrum (here only the second scattering was considered) does not hinder the extraction of the contours by a filtered back-projection type reconstruction formula. Even though, the method is sensitive to the variation of the physical factors, it constitutes an interesting and fast to implement first step to reverse the spectrum and/or provide initial conditions to more complex and expensive algorithms. Such algorithms will be the focus of our future research.

References

- [1] O. O. ADEJUMO, F. A. BALOGUN, AND G. G. O. EGBEDOKUN, *Developing a compton scattering tomography system for soil studies: Theory*, Journal of Sustainable Development and

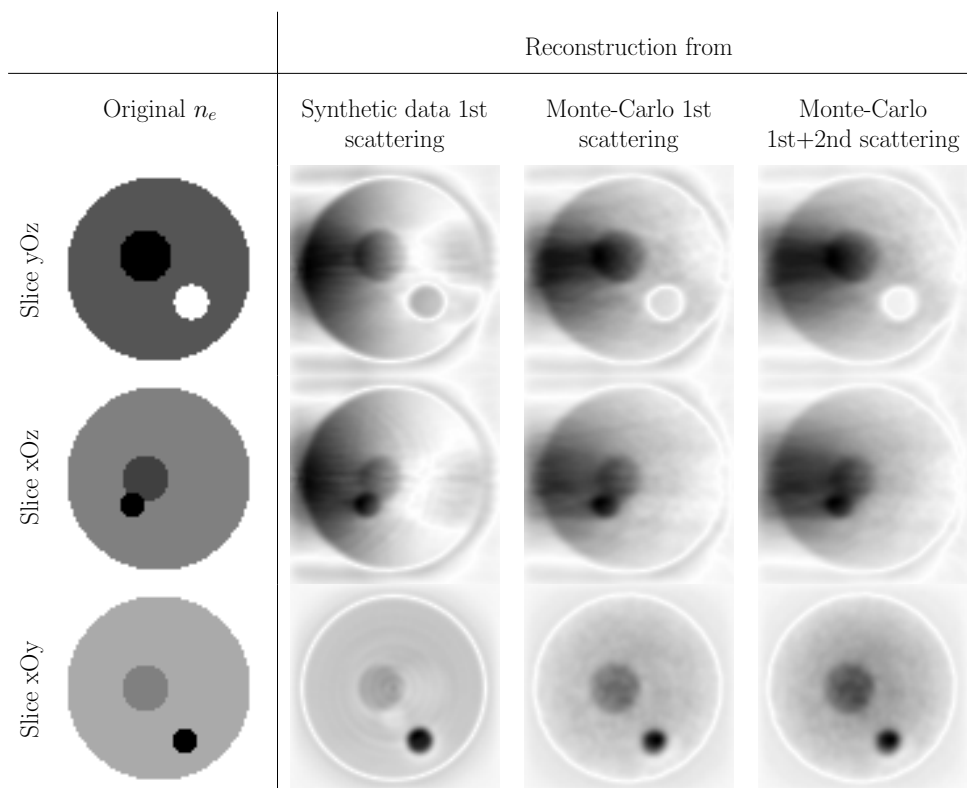


Figure 8. first column: original electron density; Columns 2 to 4: Reconstruction from g_1 , g_1^{MC} and $g_1^{MC} + g_2^{MC}$ respectively.

- Environmental Protection, 1 (2011), pp. 73–81.
- [2] R. ALVAREZ AND A. MACOVSKI, *Energy-selective reconstructions in x-ray computerized tomography*, Phys Med Biol., 21 (1976), pp. 733–744.
 - [3] S. ANGHAIE, L. L. HUMPHRIES, AND N. J. DIAZ, *Material characterization and flaw detection, sizing, and location by the differential gamma scattering spectroscopy technique. Part1: Development of theoretical basis*, Nuclear Technology, 91 (1990), pp. 361–375.
 - [4] N. V. ARENDTSZ AND E. M. A. HUSSEIN, *Energy-spectral Compton scatter Imaging - Part 1: theory and mathematics*, IEEE Transactions on Nuclear Sciences, 42 (1995), pp. 2155–2165.
 - [5] F. A. BALOGUN AND P. E. CRUVINEL, *Compton scattering tomography in soil compaction study*, Nuclear Instruments and Methods in Physics Research A, 505 (2003), pp. 502–507.
 - [6] A. BRUNETTI, R. CESAREO, B. GOLOSIO, P. LUCIANO, AND A. RUGGERO, *Cork quality estimation by using Compton tomography*, Nuclear instruments and methods in Physics research B, 196 (2002), pp. 161–168.
 - [7] R. CESAREO, C. C. BORLINO, A. BRUNETTI, B. GOLOSIO, AND A. CASTELLANO, *A simple scanner for Compton tomography*, Nuclear Instruments and Methods in Physics Research A, 487 (2002), pp. 188–192.
 - [8] R. L. CLARKE AND G. V. DYK, *A new method for measurement of bone mineral content using both transmitted and scattered beams of gamma-rays*, Phys. Med. Biol., 18 (1973), pp. 532–539.
 - [9] A. H. COMPTON, *A quantum theory of the scattering of x-rays by light elements*, Phys. Rev., 21 (1923), pp. 483–502.
 - [10] C. DRIOI, *Imagerie par rayonnement gamma diffusé à haute sensibilité*, PhD thesis, Univ. of Cergy-Pontoise, 2008.
 - [11] E. SHEFER *et al*, *State of the Art of CT Detectors and Sources: A Literature Review*, Current Radiology Reports, 1 (2013), pp. pp. 76–91.

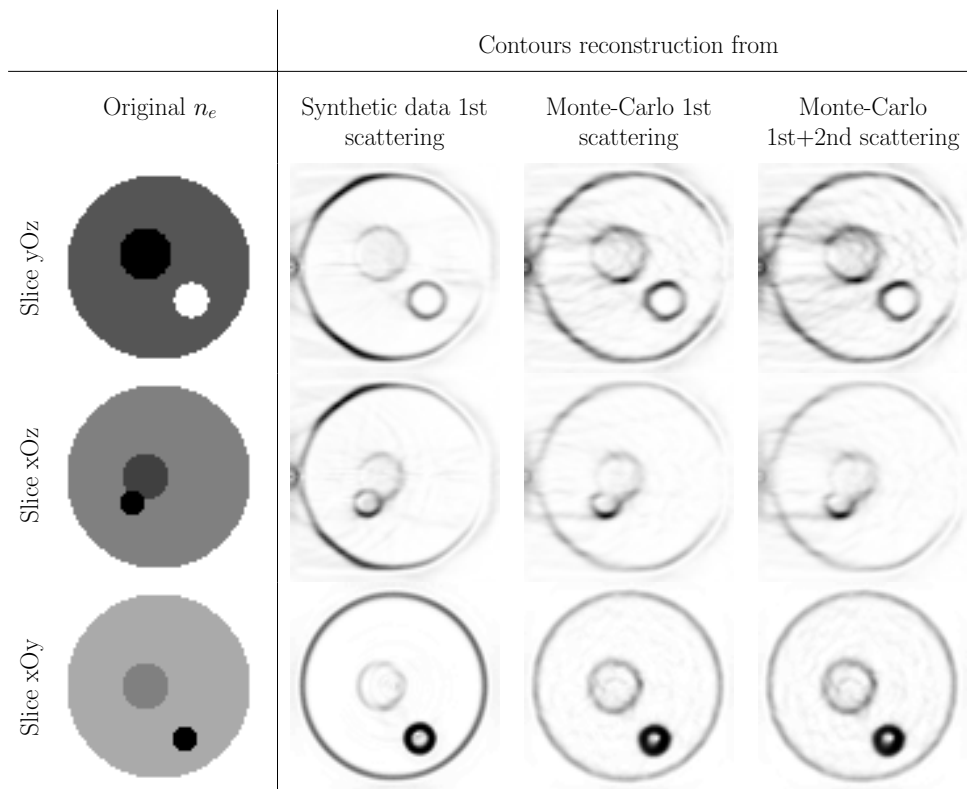


Figure 9. Corresponding gradients to the reconstructions in Figure 8.

- [12] B. L. EVANS, J. B. MARTIN, L. W. BURGGRAF, AND M. C. ROGGEMANN, *Nondestructive inspection using Compton scatter tomography*, IEEE Transactions on Nuclear Science, 45 (1998), pp. 950–956.
- [13] F. T. FARMER AND M. P. COLLINS, *A new approach to the determination of anatomical cross-sections of the body by Compton scattering of gamma-rays*, Phys. Med. Biol., 16 (1971), pp. 577–586.
- [14] E. FREDENBERG, *Spectral and dual-energy X-ray imaging for medical applications. Nuclear Instruments and Methods in Physics Research Section A: Accelerators, Spectrometers, Detectors and Associated Equipment*, 878 (2018), pp. pp 74–87.
- [15] H. GOO AND J. GOO, *Dual-Energy CT: New Horizon in Medical Imaging*, Korean J Radiol., 18 (2017), pp. pp. 555–569.
- [16] V. A. GORSHKOV, M. KROENING, Y. V. ANOSOV, AND O. DORJGOCHOO, *X-Ray scattering tomography*, Nondestructive Testing and Evaluation, 20 (2005), pp. 147–157.
- [17] R. GUZZARDI AND G. LICITRA, *A critical review of Compton imaging*, CRC Critical Reviews in Biomedical Imaging, 15 (1988), pp. 237–268.
- [18] B. HAHN AND E. QUINTO, *Detectable singularities from dynamic Radon data*, SIAM J. Imaging Sciences, 9 (2016), pp. 1195–1225.
- [19] G. HARDING AND E. HARDING, *Compton scatter imaging: a tool for historical exploitation*, Appl Radiat Isot., 68 (2010), pp. 993–1005.
- [20] G. HOUNSFIELD, *Computerized transverse axial scanning (tomography). i. description of system*, Br J Radiol., 46 (1973), pp. pp. 1016–1022.
- [21] O. KLEIN AND Y. NISHINA, *Über die Streuung von Strahlung durch freie Elektronen nach der neuen relativistischen Quantendynamik von Dirac*, Z. Phys., 52 (1929), pp. 853–869.
- [22] V. KRISHNAN AND E. T. QUINTO, *Microlocal Analysis in Tomography*, Handbook of Mathematical Methods in Imaging, Book editor: Otmar Scherzer, 2015.
- [23] P. G. LALE, *The Examination of Internal Tissues, using Gamma-ray Scatter with a Possible*

- Extension to Megavoltage Radiography*, Physics in Medicine and Biology, 4 (1959), pp. 159–167.
- [24] C. MCCOLLOUGH, S. LENG, Y. LIFENG, AND J. FLETCHER, *Dual- and Multi-Energy CT: Principles, Technical Approaches, and Clinical Applications*, Radiology, 276 (2015), pp. pp. 637–653.
- [25] D. A. MENELEY, E. M. A. HUSSEIN, AND S. BANERJEE, *On the solution of the inverse problem of radiation scattering imaging*, Nuclear Science and Engineering, 92 (1986), pp. 341–349.
- [26] M. NGUYEN, T. TRUONG, M. MORVIDONE, AND H. ZAIDI, *Scattered radiation emission imaging: Principles and applications*, International Journal of Biomedical Imaging (IJBI), (2011), p. 15pp.
- [27] S. J. NORTON, *Compton scattering tomography*, Jour. Appl. Phys., 76 (1994), pp. 2007–2015.
- [28] P. PRADO, M. NGUYEN, L. DUMAS, AND S. COHEN, *Three-dimensional imaging of flat natural and cultural heritage objects by a Compton scattering modality*, Journal of Electronic Imaging, 26 (2017), p. 011026.
- [29] A. PRIMAK, J. R. GIRALDO, X. LIU, L. YU, AND C. MCCOLLOUGH, *Improved dual-energy material discrimination for dual-source CT by means of additional spectral filtration*, Med Phys., 36 (2009), pp. pp. 1359–1369.
- [30] G. RIGAUD, *Compton Scattering Tomography: Feature Reconstruction and Rotation-Free Modality*, SIAM J. Imaging Sci., 10 (2017), p. 22172249.
- [31] G. RIGAUD AND B. HAHN, *3D Compton scattering imaging and contour reconstruction for a class of Radon transforms*, Inverse Problems, 2018 (7), p. 075004.
- [32] G. RIGAUD AND A. LAKHAL, *Approximate inverse and Sobolev estimates for the attenuated Radon transform*, Inverse Problems, 31 (2015), p. 105010.
- [33] J. P. STONESTROM, R. E. ALVAREZ, AND A. MACOVSKI, *A framework for spectral artifact corrections in x-ray CT*, IEEE Trans. Biomed. Eng., 28 (1981), pp. 128–141.
- [34] B. TRACEY AND E. MILLER, *Stabilizing dual-energy X-ray computed tomography reconstructions using patch-based regularization*, Inverse Problems, 31 (2015), p. 05004.
- [35] F. TREVES, *Introduction to pseudodifferential and Fourier Integral Operators*, Plenum Press, New York, The University Series in Mathematics, 1980.
- [36] J. WEBBER AND S. HOLMAN, *Microlocal analysis of a spindle transform*, arXiv e-prints, (2017), p. arXiv:1706.03168.
- [37] J. WEBBER AND W. LIONHEART, *Three dimensional Compton scattering tomography*, arXiv e-prints, (2017), p. arXiv:1704.03378.
- [38] J. WEBBER AND E. QUINTO, *Microlocal analysis of a Compton tomography problem*, arXiv e-prints, (2019), p. arXiv:1902.09623.